THE ASTROPHYSICAL JOURNAL, 443:231–237, 1995 April 10

ROSAT OBSERVATIONS OF THE SUPERNOVA REMNANT 3C 400.2

JON M. SAKEN AND KNOX S. LONG
Space Telescope Science Institute, 3700 San Martin Drive, Baltimore, MD 21218; saken@stsci.edu, long@stsci.edu
WILLIAM P. BLAIR
Department of Physics and Astronomy, Johns Hopkins University, Baltimore, MD 21218; wpb@pha.jhu.edu
AND
P. FRANK WINKLER
Department of Physics, Middlebury College, Middlebury, VT 05753; winkler@middlebury.edu
Received 1994 June 27; accepted 1994 October 18

ABSTRACT

We have used the *ROSAT* PSPC to examine the X-ray emission from 3C 400.2, a supernova remnant which is a member of a class of remnants with limb-brightened radio and centrally condensed X-ray morphologies. The X-ray emission fills the radio shell and is characterized by an interior peak in the northwest region of the remnant. Otherwise, the surface brightness has a relatively smooth distribution. The X-ray peak is not correlated with any radio features or with the observed optical filaments.

The PSPC X-ray spectrum is not well fitted by a power-law model but can be described in terms of thermal emission from a hot plasma with solar abundances. The only point source along the line of sight to the SNR is associated with a bright foreground F8 star. Thus the X-ray emission from 3C 400.2 is unlikely to be due to synchrotron radiation from an active pulsar. If the emission arises from a thermal plasma and the absorbimg column along the line of sight to 3C 400.2 is 7.8×10^{21} cm^{-2}, then the temperature of the plasma is 0.27 keV, and the 0.4–2.4 keV X-ray luminosity is 1.3×10^{36} ergs s^{-1} for an assumed distance of 6 kpc. An X-ray hardness ratio map shows a slight increase in the hardness of the emission in the regions of the remnant with a higher X-ray surface brightness. Assuming uniform absorption across the remnant, this increase implies the temperature is $\sim$1.5 times greater in the high surface brightness regions of the SNR.

The relatively uniform spectrum and the anticorrelation between X-ray and radio features seems to rule out the possibility that 3C 400.2 is actually two overlapping or interacting SNRs. The morphology of 3C 400.2 can be explained in terms of a multiphase ISM in which the primary shock is expanding into an ISM studded with dense cloudlets, if the clouds are evaporated or disrupted on a timescale which is long compared to the age of the SNR. It may also be possible to explain the emission in terms of the interaction of the SNR with a massive wind-driven shell, although the existing models for the evolution of a SNR in this environment suggest that the Hα luminosity should be much larger than the X-ray luminosity, which is not observed. We cannot completely rule out the possibility that 3C 400.2's appearance as a centrally peaked X-ray SNR is the result of an interaction between the remnant and a cloud along the line of sight, although this seems unlikely.

Subject headings: ISM: individual (3C 400.2) — ISM: supernova remnants — X-rays: ISM

1. INTRODUCTION

The supernova remnant (SNR) 3C 400.2 is well observed at radio, optical, and X-ray wavelengths. It was first detected as an X-ray source by Agrawal, Riegler, & Singh (1983) using the *HEAO* A-2 soft X-ray proportional counter. The *Einstein* IPC X-ray observations reported by Long et al. (1991) show that 3C 400.2 belongs to a class of SNRs that have limb-brightened radio morphologies but broad interior peaks in their X-ray emission. Other SNRs of this type include HB 3 (Venkatesan et al. 1984), HB 9 (Tuohy, Clark, & Garmire 1979), W28 (Long et al. 1991), and W44 (Rho et al. 1994). Most of these SNRs are large-diameter objects and show substantial foreground extinction. For 3C 400.2, Long et al. (1991) estimate the reddening to be $E(B-V) \sim 1.0$–1.3, or $N_{\rm H} = 7$–11×10^{21} cm^{-2} based on optical spectra of the filaments. The reason for the differences between the X-ray and radio morphologies of SNRs in this class is not well understood. Most have soft X-ray spectra, consistent with the interpretation that these are evolved remnants.

The distance to 3C 400.2 is not well known. Rosado (1983) estimates 6.7 ± 0.6 kpc, based on a systematic velocity of 96 ± 9 km s^{-1} derived from Fabry-Perot measurements. The only other distance estimates for 3C 400.2 used the highly unreliable Σ-*D* relation, and range from 3.8 (Milne 1979) to 6.3 kpc (Caswell & Lerche 1979). For the purpose of this paper we will assume a distance of 6 kpc, which most recent observers have adopted. At radio wavelengths 3C 400.2 has an elliptical, shell-like morphology, extending to the northwest, with an angular size of 33′ × 28′ (Dubner et al. 1994). At our assumed distance, this corresponds to dimensions of 58 × 49 pc.

The optical emission from 3C 400.2 consists of an incomplete shell of diffuse filaments only 16′ across (Winkler, Olinger, & Westerbeke 1993). Optical emission is not observed from the eastern half of the SNR. The optical emission tends to be seen in regions with high radio surface brightness, though the correlation is by no means exact. Some of this optical emission is distinctly filamentary, especially in the south central region, while the Hα emission near the X-ray peak is decidedly diffuse (see Blair & Long 1988). Spectra of the south central filaments by Blair & Long (1988) are typical for shock heating, with strong [S II] and [O I] emission relative to Hα. Densities derived from the [S II] (60–210 cm^{-3}) are typical of old SNRs. No optical spectra exist for the faint, diffuse emission near the X-ray peak.

Here we report a *ROSAT* PSPC study of 3C 400.2. The observations allow a detailed comparison of the X-ray morphology with new optical and radio images that have recently become available (Winkler et al. 1993; Dubner et al. 1994) and permit us to search for X-ray spectral variations as a function of position within the SNR. The observations and data reductions are presented in § 2, and a discussion of our findings is given in § 3.

2. *ROSAT* OBSERVATIONS

ROSAT and the PSPC instrument have been described by Aschenbach (1988) and Pfefferman et al. (1986). The PSPC is sensitive between 0.1 and 2.4 keV and has a peak effective area of 220 cm^2 on axis at 1 keV. The FWHM energy resolution ($\Delta E/E$) at 1 keV is 0.41 and scales as approximately $E^{-1/2}$. The PSPC field of view is about 2°; the spatial resolution is about 25″ on axis and increases to several arcminutes outside the central 40′.

A series of three PSPC pointings were obtained in order to observe the entire SNR without interference from the PSPC's circular rib structure and to allow good background measurements from regions outside the SNR boundaries. The pointing positions and observation times are listed in Table 1. As it turned out, the entire SNR fitted inside the central regions in each of the observations. All three pointings had consistent background levels with no short-term enhancements in the total count rate. The total source count rate from the SNR was about 1.3 s^{-1}.

TABLE 1

SUMMARY OF *ROSAT* PSPC POINTINGS FOR 3C 400.2

Region[a]	Observation Dates	Position (J2000) R.A.	Position (J2000) Decl.	Observation Time (s)
NW......	1992 Oct 4–10	19^{h}38^{m}24^s	17°19′48″	3570
NE	1992 Nov 3–4	19 39 29	17 20 24	2361
S.........	1992 Nov 7–9	19 39 00	17 07 48	2115

[a] Although exposures were offset, each pointing contained the entire SNR.

A composite image of 3C 400.2 is shown in Figure 1. This image was produced by transforming the three pointings onto a common coordinate system and covers the energy range 0.42–2.47 keV. Regions under the ribs were excluded by rejecting pixels with a total vignetting-corrected exposure time of less than 1000 s in each image. The total number of counts in each pixel were added, the resulting image was divided by the total vignetting-corrected exposure time (at 1 keV), and then smoothed by a Gaussian with FWHM = 1′.

The overall structure of the PSPC image resembles that obtained with *Einstein* (Long et al. 1991). However, the PSPC image shows more diffuse emission and provides improved resolution of the internal structure. The SNR is elliptical in shape with major and minor axes of 30′ and 24′. This is about

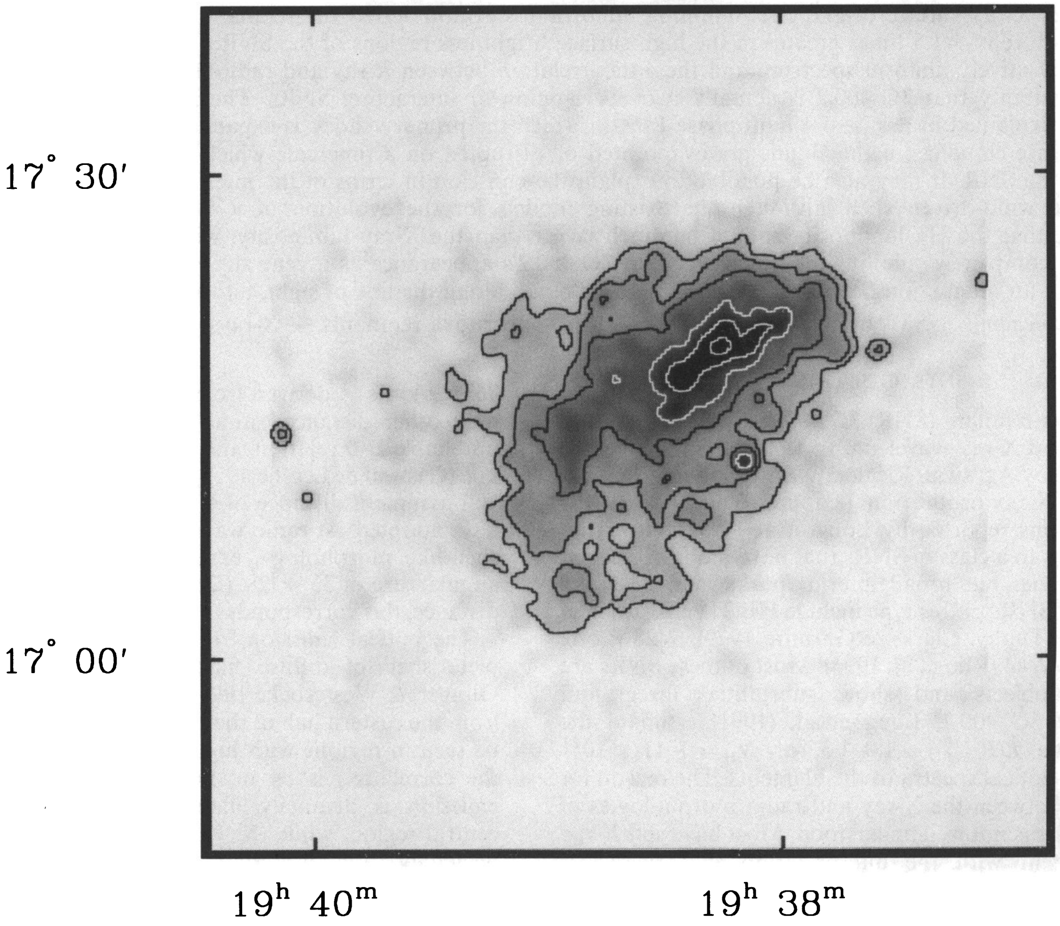

FIG. 1.—Composite PSPC image of 3C 400.2, including only those regions with a vignetting-corrected exposure of at least 1000 s in the individual pointings. The image has been flat-fielded by dividing by the total exposure time, smoothed with a 1′ Gaussian and linearly scaled from -1.7×10^{-4} to 1.3×10^{-2} s^{-1} arcmin^{-2}. Contour levels are at (1.9, 3.1, 4.9, 8.0, 11, 14) $\times 10^{-3}$ s^{-1} arcmin^{-2}. The coordinates are J2000.

1′ less than the dimensions of the corresponding region of the radio shell. Part of this difference may be due to the difficulty of determining the eastern boundary, where the X-ray emission is weakest. The X-ray surface brightness has a peak of 1.6×10^{-2} s^{-1} arcmin^{-2} at R.A. = $19^h38^m16^s$, decl. = 17°19′18″ (J2000), about midway between the geometric center and northwest edge. There is no evidence for limb-brightening near the edge of the SNR. There is some structure in the interior on a scale of 3′–5′. In particular, there appears to be a ridge of emission extending from the peak toward the southeast. The diffuse emission breaks up into a set of knots in the eastern side of the remnant. Most of these features also appear in the *Einstein* maps (see especially Fig. 3 of Winkler et al. 1993) which suggests that they are real. In an attempt to look for morphological differences at harder X-ray energies, we also constructed a map including only X-rays between 1.2 and 3.0 keV. No obvious differences were seen between this map and that shown in Figure 1.

There is no evidence for a point source at or near the peak of the X-ray emission. However, there is an X-ray point source on the western limb of the SNR at R.A. = $19^h38^m10^s$, decl. = 17°12′10″ (J2000). This source is within 1″ of a V = 9.2 F8 star, BD +16°3926. The *ROSAT* source has a soft X-ray spectrum, and a significant number of counts below 0.5 keV, consistent with its identification as a foreground star. The source is most likely much closer than 3C 400.2. Assuming the *ROSAT* source is the F8 star, its X-ray to optical flux ratio, $F_x/F_{opt} = 0.26$. F_x, was calculated from a blackbody fit to the PSPC spectrum with $T = 1.8 \times 10^6$ K. This temperature is typical for an F star corona (Schmitt 1990). The *Einstein* observations of F and G stars (Maggio et al. 1987) showed that they vary widely in their observed flux. Values of F_x/F_{opt} from this survey for F stars (excluding binaries) range from 5×10^{-3} to 0.22.

Figure 2 shows the same image as in Figure 1, with the contrast adjusted to emphasize the diffuse emission, overlaid with the radio image of Dubner et al. (1994). The X-ray emission fills the radio shell, and the outer boundaries of each are almost identical. However the X-ray and radio intensities are not well correlated, and the ridge of emission described above fills a region with low radio surface brightness. There is no increased X-ray emissivity associated with the bright radio features in the northeast and northwest. Figure 3 (Plate 1) shows the Hα + [N II] CCD image from Winkler et al. (1993) with the same PSPC contours as in Figure 1 superposed. The optical emission consists mainly of a set of filaments located in the interior of the X-ray emission along the southwest edge. The optical filaments are also not well correlated with X-ray features. In particular there is no enhanced optical emission associated with the X-ray peak or the interior ridge, although faint diffuse Hα is present near the X-ray maximum (Blair & Long 1988).

Spectra were extracted from each pointing using the IRAF/PROS analysis package. Backgrounds were taken from

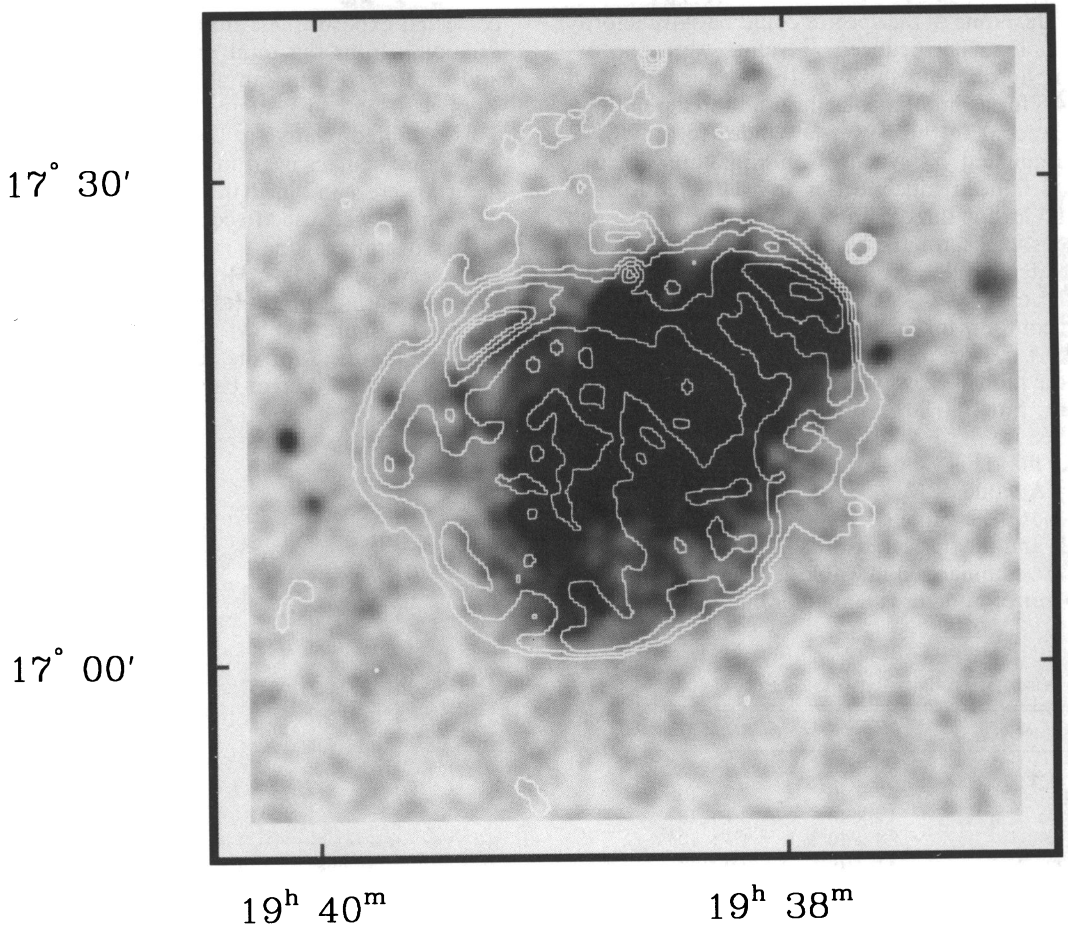

FIG. 2.—Composite PSPC image of 3C 400.2 showing the same region as in Fig. 1, with radio contours from Dubner et al. (1994). The PSPC image has been linearly scaled from -1.7×10^{-4} to 3.2×10^{-3} s^{-1} arcmin^{-2} in order to emphasize the fainter structure. Radio contour levels are at 1, 2.5, 5, 10, 15, 20 mJy beam^{-1}. The coordinates are J2000.

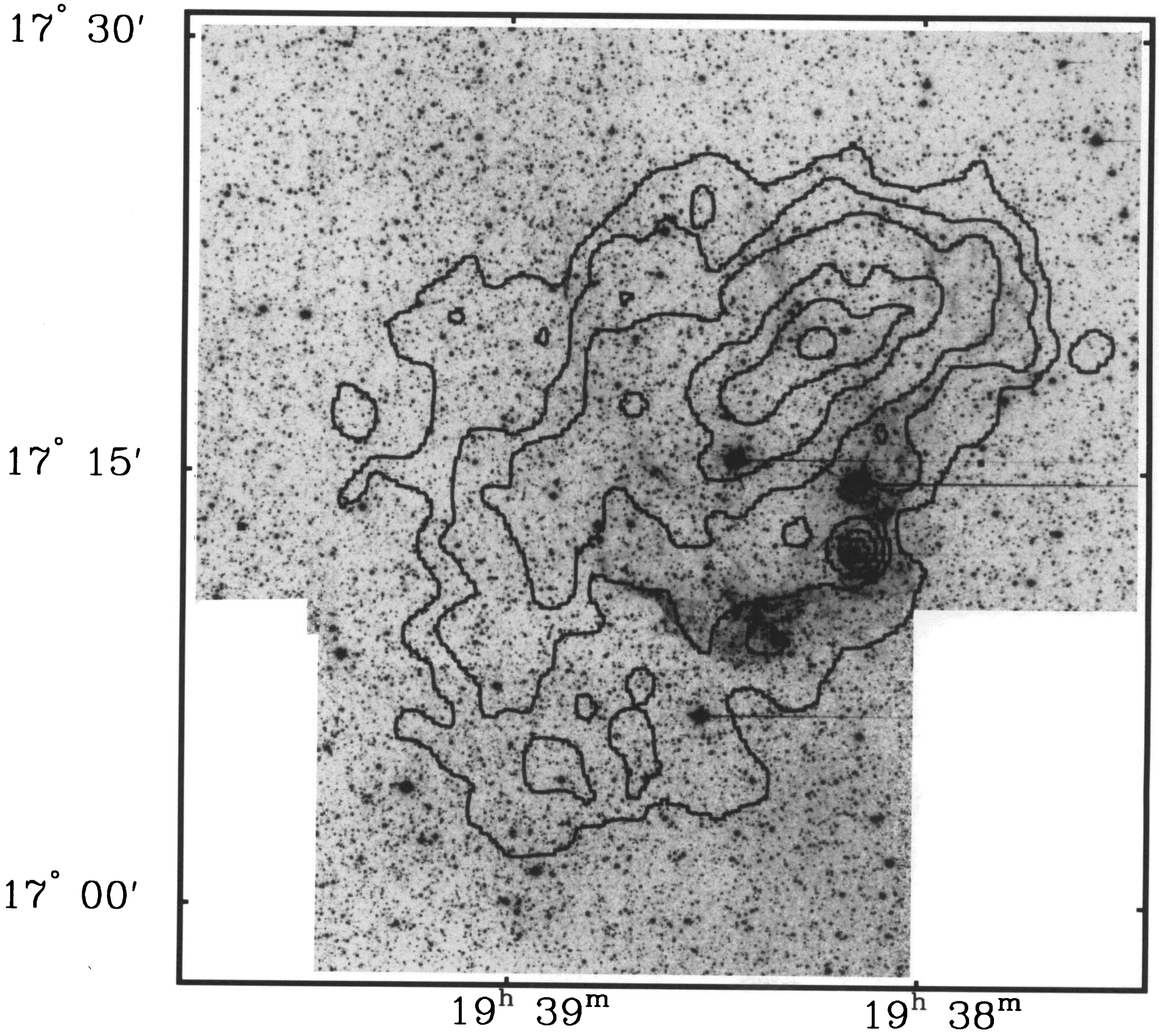

FIG. 3.—Hα + [N II] CCD image from Winkler et al. (1993) overlaid with the same PSPC image contours as in Fig. 1. The coordinates are J2000.

SAKEN et al. (see 443, 233)

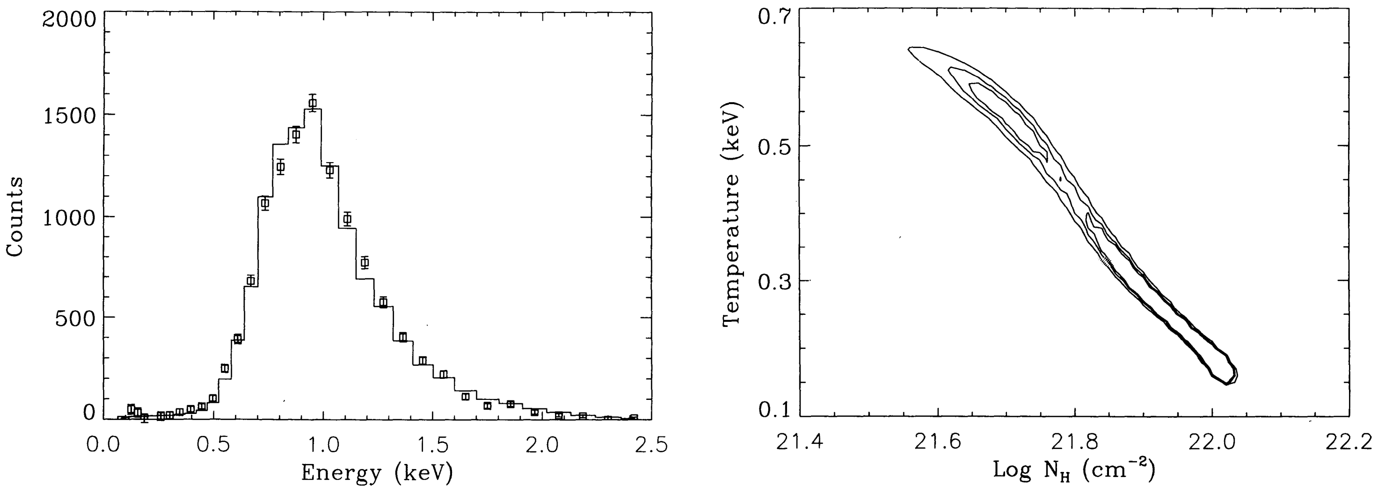

FIG. 4*a* FIG. 4*b*

FIG. 4.—(*a*) Total PSPC spectra for 3C 400.2 and (*b*) χ^2 contours at 68%, 90%, and 99% confidence intervals for a fit assuming a Raymond & Smith (1974) thermal plasma.

annular regions centered on the image center with inner and outer diameters of 29′ and 48′. Regions under the ribs were excluded from both source and background regions by filtering out pixels with vignetting-corrected exposure times less than 33% of the maximum exposure time. The point source was excluded by rejecting all pixels within a 2′ radius of the source. Fits to both power-law and Raymond-Smith (1977) thermal plasmas were made. None of the spectra could be satisfactorily fitted by a power law. The reduced χ^2 values were approximately 2–4 with photon indices of 14.2–16.2 for the individual pointings and 14.8 for a simultaneous fit to all three pointings. This is much steeper than the power-law index for any SNR known to be dominated by synchrotron emission. Thermal plasma models produced much better fits with reduced χ^2 values of 1.3 to 1.5 for the three pointings. As expected for such heavily reddened, soft spectra, the best fit values for N_H and kT are highly correlated. If $N_H = 3 \times 10^{21}$ cm^{-2}, then $kT \sim 0.7$ keV; if $N_H = 10^{22}$ cm^{-2}, $kT \sim 0.2$ keV. A summed, extracted spectrum and χ^2 contours for the fit are shown in Figure 4.

The observed 0.4–2.4 keV flux is 1.5×10^{-11} ergs cm^{-2} s^{-1}, independent of the model. However, the intrinsic luminosity is model dependent. Since a large range of the parameters is allowed by the fits, we fixed N_H at 7.8×10^{21} cm^{-2}, based on an average of the fits. This yields a fit temperature of 0.27 keV in each pointing. A value of $N_H = 7.8 \times 10^{21}$ cm^{-2} is in good agreement with both the value derived from *Einstein* data by Long et al. (1991) and the optical extinction of $E(B-V) = 1.0$–1.3. Our results are summarized in Table 2, where we assume a volume filling factor of 1 and use an angular diameter of 28′.

TABLE 2

COMPARISON OF DERIVED PARAMETERS FOR 3C 400.2

Parameter	*Einstein*[a]	*ROSAT*[a]
F (s^{-1})	0.7	1.3
N_H (cm^{-2})	7.7×10^{21}	7.8×10^{21}
T_X (K)	4.4×10^6	3.1×10^6
L_X (ergs s^{-1})	8.4×10^{34}	1.3×10^{36}
EM (cm^{-3})	3.5×10^{58}	7.0×10^{58}
n_e (cm^{-3})	0.15	0.20
m_X ($M_\odot$)	260	350

[a] 1–4 keV for *Einstein* and 0.4–2.4 keV for *ROSAT*.

In order to search for spectral variations within the remnant, we constructed a hardness ratio map, defined as (hard − soft)/(hard + soft), in 1′ bins across the entire field. For this purpose, "hard" was defined to be 0.91–2.01 keV and "soft" was defined to be 0.52–0.90 keV. First, total hard and soft energy maps were constructed from the three pointings in the same manner as was done for Figure 1. Pixels with a vignetting-corrected exposure less than 1000 s in a given pointing were excluding from the total map. Backgrounds were measured and subtracted using an annulus with inner and outer diameters of 30′ and 45′ centered at R.A. 19^{h}38^{m}27^s, decl. 17°16′40″. This is shifted relative to the center of the field so as to avoid faint point sources near the edge of the field. Then the separate images were combined into total "hard" and "soft" maps. These maps were used to construct the hardness ratio map.

The overall hardness ratio map is fairly smooth with an average value of 0.082. However, a correlation between hardness and surface brightness was evident by comparison with Figure 1. Figure 5 shows the hardness ratio as a function of surface brightness for the contour regions shown in Figure 1 along with the 1 σ error bars. The regions between 1.2×10^{-4}

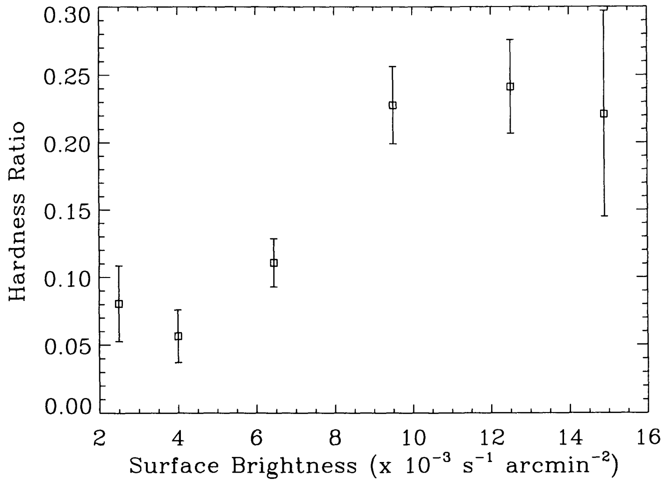

FIG. 5.—Hardness ratio as a function of X-ray surface brightness for the contour regions shown in Fig. 1

and 5×10^{-4} s^{-1} have an average hardness ratio of 0.083 ± 0.012 and regions brighter than 5×10^{-4} s^{-1} have an average value of 0.24 ± 0.02. Assuming the best-fit column density of 7.8×10^{21} cm^{-2}, these hardness ratios correspond to temperatures of 0.23 keV and 0.36 keV. We cannot rule out the possibility that the apparent variations in temperature are actually due to spatial variations in the absorbing column; a relatively small change of 36% in the absorbing column would be required. However, it seems unlikely that the low surface brightness regions of the SNR would have the smaller absorbing column. Hence, we favor the interpretation that the temperature is higher in the regions with higher-X-ray surface brightness.

3. DISCUSSION

A variety of environmental factors probably contribute to the X-ray morphology of the SNRs with interior-peaked X-ray and limb-brightened radio morphologies, since the appearance of this "class" of SNRs is heterogeneous. In fact, a number of models have been used to explain the X-ray emission from these remnants. *Einstein* observations of HB 21 by Leahy (1987) show a significant amount of interior X-ray emission that is poorly correlated with the radio emission. He invokes a three-component ISM model (Cowie, McKee, & Ostriker 1987) to explain its structure, which would be similar in many respects to the evaporating cloudlets model of White & Long (1991). HB3 was also observed with *Einstein* (Leahy et al. 1985). These observations revealed a bright inner ring and significant temperature variations, with the highest temperatures found in the center of the remnant. They concluded that its structure was most likely result of a second SNR in the center, a preexistent stellar wind bubble, or a reverse shock. No evidence was seen for a plerionic component. Finally, Rho et al. (1994) find a centrally peaked X-ray morphology for W44 that is consistent with an evaporating cloud model (White & Long 1991). Although W44 is known to have an active pulsar, no evidence for it is seen in the *ROSAT* image.

The combination of an inhomogeneous interstellar medium and projection effects can make the three-dimensional structure of an evolved SNR difficult to disentangle, complicating the physical interpretation. A case to consider is VRO 42.05.01, recently observed with *ROSAT* by Burrows & Guo (1994). At radio wavelengths, this remnant consists of a "shell" intersected by a much larger curved component, or "wing." The remnant has apparently broken out of the cloud in which the SN occurred (Pineault, Landecker, & Routledge 1987), expanded across a cavity, and is now interacting with the material forming the opposite wall. The X-ray emission is not limb brightened. Instead, it fills the wing and shell, and peaks inside the wings, coincident with a neutral cloud observed at 21 cm (Landecker et al. 1989). If the line of sight to VRO 42.05.01 was rotated ~90° with respect to our current viewing angle, we would see the shell projected against the wing (or the wing projected against the shell). In this case the remnant's X-ray morphology would appear to be an elliptical SNR with an interior peak.

The main characteristics of the X-ray emission from 3C 400.2 are a relatively smooth X-ray surface brightness distribution peaking inside the radio shell and a fairly homogeneous temperature distribution. The absence of strong spatial structure and a central point source suggest that the interior of the SNR is filled with X-ray emitting material. This morphology is not, as was pointed out by Long et al. (1991), easy to explain in terms of an explosion in a uniform density ISM, even in the presence of overlying absorption, because the SNR shock sweeps out the interior of the SNR leading to a limb-brightened X-ray morphology. In the discussion that follows we will assume that the X-ray emission in 3C 400.2 is actually located in the interior of the SNR. We believe this is reasonable in view of the fact that the radio and X-ray surface brightness distributions are so different. If, for example, there was a large gradient in the density along the line of sight, then one might expect the radio and X-ray surface brightness distribution to be more similar.

The X-ray emission from 3C 400.2 is unlikely to be produced by emission from an active pulsar. The only X-ray point source along the line of sight to 3C 400.2 has an X-ray spectrum that is consistent with its identification as a foreground F star. Unlike SNRs dominated by pulsars, the X-ray spectrum of 3C 400.2 is poorly fitted by a power-law model and the required power law index is much steeper than that of any pulsar-dominated SNR. The spectrum is well-fit in terms of a thermal plasma with an energy content of $\sim 4 \times 10^{50}$ ergs.

Long et al. (1991) interpreted *Einstein* observations of the X-ray emission from 3C 400.2 in terms of a model in which dense cloudlets survived the passage of the shock wave and subsequently evaporated in the SNR interior. They based their interpretation on a similarity solution for SNRs evolving in a cloudy ISM developed by White & Long (1991). The similarity solution exists as long as the evaporation rate scales inversely as the age of the SNR, which is approximately the scaling for saturated conduction (see, e.g., Cowie et al. 1981). The similarity solution depends on two dimensionless parameters: C, the cloudlet to intercloud mass ratio, and τ, the ratio of the cloud evaporation time to remnant age. Long et al. (1991) found that if the mass of material in the dense cloudlets was large compared to that in the intercloud medium, and if the evaporation time of the clouds was approximately 20–30 times the age of the SNR, then the X-ray surface brightness appears centrally peaked. In the limit in which both C and τ are large compared to 1, then the solution only depends on the ratio of C to τ. Assuming that the ratio of C/τ was 3 and that the explosion energy for 3C 400.2 was 10^{51} ergs, Long et al. found that the observed luminosity could be explained if 3C 400.2 was a 15,000 yr old SNR expanding into a medium with a density of 0.04 cm^{-3}. The emission measure-averaged temperature for the X-ray emitting gas would be about 5×10^6 K, close to the value we measure with *ROSAT*. The temperature variation as a function of radius for such a model is small and would not have been detected with *ROSAT*.

There should be Hα (and IR) emission associated with the clouds. If evaporating clouds are the dominant source of Hα emission in 3C 400.2, then (for the parameters chosen by Long et al.) one would expect emission to be less peaked that the X-ray emission and to appear over the entire face of the SNR. Although there does appear to be diffuse emission near the X-ray bright center of the SNR (Blair & Long 1988), the optical and X-ray emission from 3C 400.2 are not well correlated. This may not be a major problem for the evaporation model, however. Using equation (36) of White & Long (1991) and assuming an average cloud size of 1 pc, we estimate the expected Hα luminosity from cloudlet evaporation to be $< 10^{35}$ ergs s^{-1}. On the other hand, Winkler et al. (1993) estimate the Hα luminosity of 3C 400.2 to be 3×10^{35} ergs s^{-1}. Thus it is possible that the overall Hα emission arising from the primary shock can hide the emission expected from the evaporating cloudlets.

Another mechanism which can disrupt clouds in the interior is the SNR shock. Early numerical studies (Sgro 1975; Woodward 1976) lacked sufficient resolution to follow the shocks inside a cloud and could not follow the final destruction of the cloud. Recently however, Klein, McKee, & Colella (1994) have modeled a shock-cloud interaction using an adaptive mesh technique to achieve higher resolutions. They find that a combination of Kelvin-Helmholtz and Rayleigh-Taylor instabilities do eventually destroy clouds, but that the time involved is about 3.5 "cloud-crushing times," where $t_{cc} = \chi^{1/2} a_0 / v_b$. χ is the cloud to intercloud density, a_0 is the initial cloud radius, and v_b is the shock velocity in the intercloud medium. This number is valid for $\chi = 10$–100. Typical values of t_{cc} for $\chi = 100$ are of order several thousand years. Thus a cloud could survive for on order 10^4 yr before disruption, sufficient time to make it into the interior of a SNR. For a Sedov model, the blast wave velocity scales as the age, $t^{-3/5}$, close to the scaling required for the similarity solution discussed by White & Long (1991), and therefore qualitatively one might expect similar X-ray morphologies.

If either cloudlet evaporation or cloudlet disruption are to explain the centrally condensed morphology of 3C 400.2 and other similar SNRs, however, the ISM must be full of clouds that dominate the mass of the ISM, as McKee & Ostriker (1977) originally proposed. Such dense clumps have been observed in ^{13}CO observations of the Rosette molecular cloud (Blitz 1987; Blitz & Stark 1986) down to the limiting resolution of 0.7 pc with density contrasts of 100–500. Most of the mass resides in the clumps with no more than 50% and more likely 10%–25% in the interclump medium. Evidence for large dense clumps has also been reported in the Orion molecular cloud complex (Bally et al. 1987) and the dark cloud L1624 (Margulis & Lada 1986). However, there is no indication that 3C 400.2 is associated with a molecular cloud, either from the optical or in the CO survey of Dame et al. (1987). It is unclear if such clumps are a common feature of the ISM.

For a strong shock wave propagating in a uniform density ISM, the shock effectively sweeps up the ISM and creates a limb-brightened SNR. However, the most probable prognenitors for Type II SN's are massive stars. The winds from these stars can create massive wind-driven shells with radii of 10–30 pc. Such shells have been observed at a variety of wavelengths around stars in the Milky Way (Chu, Treffers, & Kwitter 1983; Dufour 1989), and the LMC (Goudis & Meaburn 1978; Meaburn 1980; Chu & Kennicutt 1988; Rosado 1989). The existence of a massive shell alters the appearance of a SNR dramatically, as calculations by Tenorio-Tagle et al. (1990, 1991) have shown, and Dubner et al. (1994) have suggested this is one way to explain the morphology of 3C 400.2. In particular they note that this scenario is consistent with the arclike radio features they observe in the interior of the remnant.

Tenorio-Tagle et al.'s (1990) Case 2 is particularly instructive for 3C 400.2. In this model, the progenitor star injects 6 $M_\odot$ into an ISM with a density assumed to be 1 cm^{-3}. The wind sweeps out and stores 259 $M_\odot$ into a thin shell with a radius of 15 pc, before exploding. The interactions with the shell slow the primary shock considerably as it attempts to traverse the shell and generate reflected shocks that prevent the evacuation of the interior region and produce an X-ray surface brightness distribution characterized by a centrally brightened SNR. The distribution is in fact not as smooth as observed in 3C 400.2 and the effective temperature is somewhat higher. In addition, the Hα luminosity appears to be $\sim$100 times the X-ray luminosity. This is certainly not the case in 3C 400.2. Nevertheless, it seems likely that the effects of the progenitor star on the surrounding ISM play an important role in 3C 400.2 and other interior-brightened SNRs.

Dubner et al. (1994) also suggest that the optical and radio morphology of 3C 400.2 could be the result of two overlapping SNRs. The smaller (12 pc) diameter shell surrounds the high surface brightness part of the X-ray emission from 3C 400.2, while the larger (19 pc) diameter shell is located to the southeast. It is unlikely that there are two noninteracting SNRs at about the same distance. If there were, one would expect substantial temperature differences since for a SNR in the adiabatic phase, $T \propto R^{-3}$. If we assume that the two SNRs are each in the adiabatic phase, that they had similar explosion energies, and that they are expanding into an ISM of similar density, then the effective temperatures ought to be different by a factor of 4. For the specific case of E_0 of 1×10^{51} ergs and $n_{\rm ISM}$ of 0.1, the resulting temperatures are 9.2×10^6 K and 3.6×10^7 K, assuming a Sedov-Taylor similarity solution, angular diameters of 22′ and 14′ from Dubner et al. (1994) and a distance of 6 kpc. For $N_{\rm H} = 7 \times 10^{21}$ cm^{-3}, the two SNRs should produce spectra with a peak separated by 0.2 keV. This is not observed. Therefore it is unlikely that the morphology of 3C 400.2 is due to two SNRs superposed along our line of sight.

The hypothesis that 3C 400.2 consists of two interacting SNRs is more difficult to rule out, largely because there is no consensus about how to identify such SNRs. Bodenheimer, Yorke, & Tenorio-Tagle (1984) have carried out two-dimensional hydrodynamical simulations of interacting SNRs expanding into an ISM with a density of 1 cm^{-3}. They calculate models where the secondary SN explodes both inside and outside the first remnant. Models with a secondary explosion at the center of the first remnant produce composite remnants that are virtually indistinguishable from single SNRs and do not resemble 3C 400.2 Models with a second explosion outside the primary remnant produce asymmetrical composite remnants. The temperature peak is offset from the center of the composite. Of particular interest is their Case 4, with a secondary explosion occurring within the shell of the primary remnant. The second SN occurs 1.37×10^4 yr after the first SN, which has reached a size of 16 pc. At 8.7×10^4 yr after the first SN, the 1 keV X-ray map for the composite has a morphology remarkably similar to 3C 400.2. However, the model predicts larger temperature variations than we observe. A peak of 3×10^6 K occurs at the center of the second SN and declines rapidly a short distance away. This should have been readily apparent in our PSPC spectra and hardness maps. Also, only a small amount of material is added to the interior of the remnant, while the *ROSAT* data implies the interior of 3C 400.2 is relatively dense. Thus this particular model also fails to explain the X-ray properties of 3C 400.2.

In summary, the new *ROSAT* observations of 3C 400.2 have provided a higher signal-to-noise ratio X-ray map of this centrally peaked X-ray SNR. The X-ray spectrum is well fitted in terms of a thermal plasma with cosmic abundances and a temperature of 0.27 keV. The spectrum is fairly uniform across the face of the SNR, with a small increase in hardness ratio near the X-ray–bright northwest peak. The spectrum is not consistent with that expected from a synchrotron-dominated SNR and the lack of large temperature variations across the remnant argues against interaction or overlapping SNRs as an explanation for the interior-peaked X-ray morphology of 3C 400.2. Although the interaction of a progenitor's wind-driven shell with the SN blast wave could produce the X-ray peak, the lack of correlated Hα emission may pose some problems for this explanation. A model involving small evaporating clouds is consistent with the *ROSAT* observations.

We are grateful to Daniel Wang for advice on the *ROSAT* PSPC and Steve Snowden for advice on background subtraction. This research has made use of the SIMBAD database operated at CDS, Strasbourg, France. This work has been supported by NASA under grant NAG 5-1969 to STScI. W. P. B. acknowledges support from NASA grant NAG 5-1537 to JHU. P. F. W. acknowledges the support of the NSF through grants AST 91-14935 and AST 93-15967.

REFERENCES

Aschenbach, B. 1988, Appl. Opt., 27, 1404
Agrawal, P. C., Riegler, G. R., & Singh, K. P. 1983, Ap&SS, 89, 279
Bally, J., Stark, A. A., Wilson, R. W., & Langer, W. D. 1987, ApJ, 312, L45
Blair, W. P., & Long, K. S. 1988, PASP, 100, 461
Blitz, L. 1987, in Physical Processes in Interstellar Clouds, ed. G. E. Morfill & M. Scholer (Dordrecht: Reidel), 437
Blitz, L., & Stark, A. A. 1986, ApJ, 300, L89
Bodenheimer, H., Yorke, H. W., & Tenorio-Tagle, G. 1984, A&A, 138, 215
Burrows, D. N., & Guo, Z. 1994, ApJ, 421, L19
Caswell, J. L., & Lerche, I. 1979, MNRAS, 187, 201
Chu, Y.-H., & Kennicutt, R. C., Jr. 1988, AJ, 96, 1874
Chu, Y.-H., Treffers, R. R., & Kwitter, K. B. 1983, ApJS, 53, 937
Cowie, L. L., McKee, C. F., & Ostriker, J. P. 1981, ApJ, 247, 908
Dame, T. M., et al. 1987, ApJ, 322, 706
Dubner, G. M., Giacani, E. B., Goss, W. M., & Winkler, P. F. 1994, AJ, 108, 207
Dufour, R. J. 1989, Rev. Mexicana Astron. Af., 18, 87
Goudis, C., & Meaburn, J. 1978, A&A, 68, 169
Klein, R. I., McKee, C. F., & Colella, P. 1994, ApJ, 420, 213
Landecker, T. L., Pineault, S., Routledge, D., & Vaneldik, J. F. 1989, MNRAS, 237, 277
Leahy, D. A. 1987, MNRAS, 228, 907
Leahy, D. A., Venkatesan, D., Long, K. S., & Naranan, S. 1985, ApJ, 294, 183
Long, K. S., Blair, W. P., White, R. L., & Matsui, Y. 1991, ApJ, 373, 567
Maggio, A., et al. 1987, ApJ, 315, 687
Margulis, M., & Lads, C. J. 1986, ApJ, 309, L87
McKee, C. F., & Ostriker, J. P. 1977, ApJ, 218, 148
Meaburn, J. 1980, MNRAS, 192, 365
Milne, D. K. 1979, Australian J. Phys., 32, 83
Pfeffermann, E., et al. 1986, Proc. SPIE, 733, 519
Pineault, S., Landecker, T. L., & Routledge, D. 1987, ApJ, 315, 580
Raymond, J. C., & Smith, B. H. 1977, ApJS, 35, 419
Rho, J.-H., Peter, R., Schlegel, E. M., & Hester, J. 1994, ApJ, 430, 757
Rosado, M. 1983, Rev. Mexicana Astron. Af., 8, 59
———. 1989, Rev. Mexicana Astron. Af., 18, 105
Schmitt, J. H. M. M. 1990, ApJ, 365, 704
Sgro, A. G. 1975, ApJ, 197, 621
Tenorio-Tagle, G., Bodenheimer, P., Franco, J., & Różyczka, M. 1990, MNRAS, 244, 563
Tenorio-Tagle, G., Różyczka, M., Franco, J., & Bodenheimer, P. 1991, MNRAS, 251, 318
Tuohy, I., Clark, R., & Garmire, G. P. 1979, MNRAS, 189, 59
Venkatesan, D., Leahy, D. A., Galas, C. M. F., Naranan, S., & Long, K. 1984, MNRAS, 208, 25
White, R. L., & Long, K. S. 1991, ApJ, 373, 543
Winkler, P. F., Olinger, T. M., & Westerbeke, S. A. 1993, ApJ, 405, 608
Woodward, P. R. 1976, ApJ, 207, 484